Continental Shelf Research 236 (2022) 104679

Contents lists available at ScienceDirect

Continental Shelf Research

journal homepage: www.elsevier.com/locate/csr

Contrasting internal tide turbulence in a tributary of the Whittard Canyon

Hans van Haren *, Furu Mienis, Gerard Duineveld

Royal Netherlands Institute for Sea Research (NIOZ), P.O. Box 59, 1790, AB Den Burg, the Netherlands

ARTICLE INFO

Keywords:
Large internal tide
Wave breaking
Sediment resuspension
Distinct difference over short distance
High-resolution observations
Whittard canyon

ABSTRACT

Submarine canyons that incise continental slopes are considered an important conduit for transport of suspended matter between shelf seas and deep-ocean. However, the exact mechanisms influencing matter transport and deposition are still largely unknown. We present moored observations of current flows, acoustic echo intensity and, in high-resolution, temperature variation from two contrasting mooring sites 6.5 km apart horizontally in 790 and 1130 m water depth in one of the tributaries incising the flank of the easternmost branch of Whittard Canyon, North-East Atlantic Ocean. The shallow site is situated on a steep thalweg slope which is supercritical for semidiurnal internal tides that have >100 m amplitudes and turbulent overturning evenly distributed over the 240 m range of observations, with no particular intensification near the seafloor. In contrast, the deep site is located on an along-canyon slope that is approximately critical for semidiurnal internal tides, with steeper slopes up-canyon and to the sidewalls. The internal tide amplitude at the deep site is about 75 m. In the lower 100 m, flow intensifies and becomes more rectilinear along the canyon axis, together with intensifying mean turbulence dissipation rate and tidally-averaged down-canyon flow. Over a semidiurnal tidal period three episodes of relatively large turbulence are observed. Turbulence is largest when an upslope moving bore passes. Smaller but still relatively large turbulence is associated with a secondary upslope bore and with strong convective overturning during the downslope tidal phase. The convection is clearly distinguished in temperature variance spectra between the buoyancy and Ozmidov frequencies, the range in which anisotropic stratified turbulence is expected. Averaged over the entire depth-time series, mean turbulent kinetic energy dissipation amounts to 4.4 $\pm$ 2 $\times$ 10^{-7} m^2 s^{-3}, equal for both sites. In the tributary, the first upslope moving bore and the convective overturning at the deep site will affect sediment resuspension most.

1. Introduction

Ocean seafloor topography form important boundaries where matter can be resuspended and different water masses are mixed. Large-scale flows may be intensified and ocean-interior 'internal' waves that are supported by the usually stable density stratification may break over topography (e.g., Thorpe, 1987). Of the various types of topography, submarine canyons incising the continental slope are especially interesting because they 'match' internal waves and turbulent motions in their complex three-dimensional structure. Nearby varying sloping topography of various scales may lead to complex reflection and focusing of internal waves (Petruncio et al., 1998; St. Laurent et al., 2001; Vlasenko et al., 2016), resulting in, for instance, intensification of flows near the seafloor and turbulent resuspension of matter. In this paper we are interested in the detailed structure of near-bottom turbulence and internal wave deformation in a tributary of the Whittard canyon on the Celtic shelf edge (Lo Iacono et al., 2020), in an area where semidiurnal tides dominate internal wave energy.

Submarine canyons are known to act as conduits for matter and associated compound transport from the productive continental shelfs to the food limited deep sea. Various processes have been identified for the episodic and continuous transport of (organic) matter varying from tidal currents, internal waves, storms, cascading events and anthropogenic activities like trawling (Palanques et al., 2009; Puig et al., 2014; Maier et al., 2019). The transport of (organic) matter through submarine canyons and the subsequent deposition has important implications for the benthic fauna thriving in these systems (Vetter et al., 2010; Robertson et al., 2020), as well as on the carbon cycle if organic matter is rapidly buried and withdrawn (Masson et al., 2010). Internal waves, which have been observed in many submarine canyons globally (for an overview Puig et al., 2014), cause periodic resuspension and dispersal of matter and are typically associated with the presence of nepheloid layers. These layers with elevated concentration of suspended particulate matter form pathways of lateral matter transport and can contribute

* Corresponding author.
E-mail address: hans.van.haren@nioz.nl (H. van Haren).

https://doi.org/10.1016/j.csr.2022.104679
Received 26 August 2021; Received in revised form 27 January 2022; Accepted 10 February 2022
Available online 12 February 2022

to the accumulation and focusing of matter in particular canyon areas (Gardner, 1989; Wilson et al., 2015). From observations along a ship-borne CTD-transect and current meters and transmissometers moored at 5 m above the seafloor at three sites in Baltimore Canyon, Gardner (1989) inferred that sediment resuspension occurred under upslope moving [internal tidal] bores that were followed by seaward isopycnal transport into the interior forming nepheloid layers.

Although large-scale internal waves are generated at the Celtic shelf break via cross-slope tidal flow (Pingree et al., 1986), the direction of propagating internal waves onto the shelf is quite random (Holt and Thorpe, 1997). This random propagation direction indicates effects of three-dimensional topography of the submarine canyons, also affecting near-surface solitary high-frequency internal waves (Vlasenko et al., 2014).

Deeper down, numerical modeling efforts demonstrate semidiurnal-tidal-baroclinic enhanced near-bottom flow, and higher available potential energy around near-critical bottom slope angles along the thalwegs (Aslam et al., 2018), with the suggestion of small-scale larger-energy spots when the slope angle of the seafloor is supercritical for internal tides.

Slope criticality occurs when the slope to the horizontal of energy beams of propagating internal waves matches that of the seafloor slope γ. As propagating internal wave frequencies (σ) are generally found in the range $f \leq \sigma \leq N$, their beam slopes β depend on local f, N and σ: $\beta = \sin^{-1}((\sigma^2\text{-}f^2)^{1/2}/(N^2\text{-}f^2)^{1/2})$, e.g. Leblond and Mysak (1978). A seafloor slope is supercritical when $\gamma > \beta$, steeper than the internal waves of interest. A seafloor slope is subcritical when $\beta > \gamma$.

On basis of geological data it has been suggested that around such depths where more internal wave energy reaches the seafloor the net transport of suspended matter is up-canyon (Gardner, 1989; Amaro et al., 2016). This may be related to the fate of upslope propagating internal tidal bores (Gardner, 1989) that have thus far been mainly studied in detail over two-dimensional large-scale slopes (e.g., Klymak and Moum, 2003; Hosegood et al., 2004). It was found that the sediment resuspension on such large-scale slopes is associated with internal wave breaking and not with (tidal) flow friction over the seafloor, as has been confirmed in (frictionless) models (e.g., Gemmrich and Klymak, 2015). The frictional law-of-the-wall is thus not applicable in case of effects of internal wave breaking over sloping topography.

In a historic wedge-shaped laboratory model without rotation, internal waves incoming from offshore demonstrated most turbulence generation in the apex, where the modelled bottom slope met the water surface, when moving over sub-critical (smaller seafloor-than internal-wave-) slopes (Cacchione and Wunsch, 1974). Canyons are thought to trap internal waves from above and outside the canyon, through reflection from the super-critical (larger seafloor-than internal-wave-) slopes, and channel and trap the energy toward the canyon floor and head (Gordon and Marshall 1976; Hotchkiss and Wunsch 1982). More recently, models and observations over quasi two-dimensional large--scale underwater topography like over large seamounts showed the tendency of more intense nonlinear internal-wave-induced turbulent overturning at just super-critical internal (tidal) wave slopes (e.g., Lamb, 2004; van Haren, 2006; Aucan et al., 2006; van Haren et al., 2015; Winters, 2015). Some observations showed intense turbulence over sloping seafloors not at all related with internal wave slope-criticality in areas of topographically trapped waves (van Haren et al., 2014). The effects of bottom slope angle on internal wave turbulence generation may be different in three-dimensional canyons however, either due to the proximity of steeper sloping sidewalls (Vlasenko et al., 2016), or due to reflection of internal tide energy at steeper super-critical up-canyon walls (Nash et al., 2004; Zhao et al., 2012; Hall et al., 2014). Possibly, although perhaps less likely in small canyons, the effects of cross-canyon ridges being a dominant turbulence generation mechanism (Thurnherr et al., 2020) may also play (a secondary) role.

In this paper we present a short (two-day) overlapping period of two identical heavily instrumented lines that were moored in a short distance from each other in a tributary of the easternmost canyon branch of Whittard Canyon. The moorings carried acoustic profilers and high-resolution temperature sensors. We focus on the detailing of the difference in internal tide wave, energy, turbulence and character between the two sites.

2. Materials and methods

A total of 242 'NIOZ4' self-contained temperature 'T' sensors are used sampling at 1 Hz, with precision better than 5×10^{-4} °C and a noise level of about 6×10^{-5} °C (van Haren, 2018). The T-sensors are taped at 2.0 m intervals to two 245 m long, 0.0063 m diameter nylon-coated steel cables. 19 T-sensors showed various electronic (noise, calibration) problems and are not further considered. These data gaps were interpolated. The T-sensors are synchronized via induction every 4 h. Thus, each entire vertical profile of 240 m is measured with a variation of less than 0.02 s.

The two instrumented cables are used in two identical sub-surface taut-wire moorings. In each of the moorings, the lowest sensor was placed 7 m above the seafloor just above the acoustic releases and the upper about 70 m below a single elliptic floatation providing 3 kN of net buoyancy. The float held a downward looking 75 kHz Teledyne-RDI Longranger Acoustic Doppler Current Profiler (ADCP) that sampled water-flow currents and acoustic echo intensity at a rate of once per 120 s in 5 m vertical bins. The ADCP has four acoustic beams that are slanted at an angle of 20° to the vertical. The current components are averaged over the four beams per depth level, i.e., over horizontal distances between 15 and 200 m. For typical current speeds of 0.25 m s^{-1}, the 1-Hz sampling rate of the T-sensors represents a 0.25 m horizontal scale resolution. The T-sensor data thus have more than 100 times better resolution of internal wave – turbulence characteristics than the ADCP-data.

The moorings were deployed at 48° 36.48′N, 9° 51.42′W, 1130 m water depth, mooring '1d(eep)', and 48° 38.28′N, 9° 47.40′W, 790 m water depth, mooring '2s(hallow)', in a tributary of the easternmost canyon branch of Whittard Canyon, Bay of Biscay, NE-Atlantic Ocean (Fig. 1) in mid-May 2018. The presence of tributaries that connect the interfluves at shallower depths with the main canyon thalweg are a prominent feature of the eastern flank of this canyon branch (Fig. 1). The two moorings were more or less located on the central axis, the thalweg, of the tributary, and were placed 6.5 km apart horizontally. On 1-km scales, the local along-canyon bottom slope angles are about >3° and ~1.7° for 2s and 1d, respectively. The nearby canyon-sidewalls have angles >3°. Due to the high (fisheries) risk in the area and adverse weather conditions the moorings were not left unattended and they were recovered before the end of the eight-day cruise. Therefore, their records overlap by two days only.

The moored observations are supported by shipborne SeaBird Electronics SBE-911 Conductivity Temperature Depth CTD-profiles which were aligned on a transect along the axis of the side branch, to within 1 km from the mooring sites. The CTD-data are used to establish a local, preferably linear, temperature-density relationship to be able to compute turbulence values from the moored high-resolution T-sensor data (van Haren and Gostiaux, 2012). In addition, the CTD was equipped with a Wetlabs FLNTU to measure turbidity and fluorescence.

During post-processing, the T-sensor data are converted to Conservative Temperature (Θ) values (IOC et al., 2010) mainly to correct for pressure compressibility effects. Over a range of 300 m above the seafloor, Θ are used as a tracer for variations in potential density anomaly referenced to a level of 1000 dbar (σ_1) following a reasonably tight, constant linear relationship obtained from CTD-data (Fig. 2),

$$\delta\sigma_1 = \alpha_1\delta\Theta, \text{ for mooring 1d with } \alpha_1 = -0.127 \pm 0.003 \text{ kg m}^{-3}\text{°C}^{-1}, \quad (1)$$

$$\delta\sigma_1 = \alpha_2\delta\Theta, \text{ for mooring 2s with } \alpha_2 = -0.19 \pm 0.01 \text{ kg m}^{-3}\text{°C}^{-1}, \quad (2)$$

in which $\alpha_{1,2}$ denote regression coefficients under local conditions

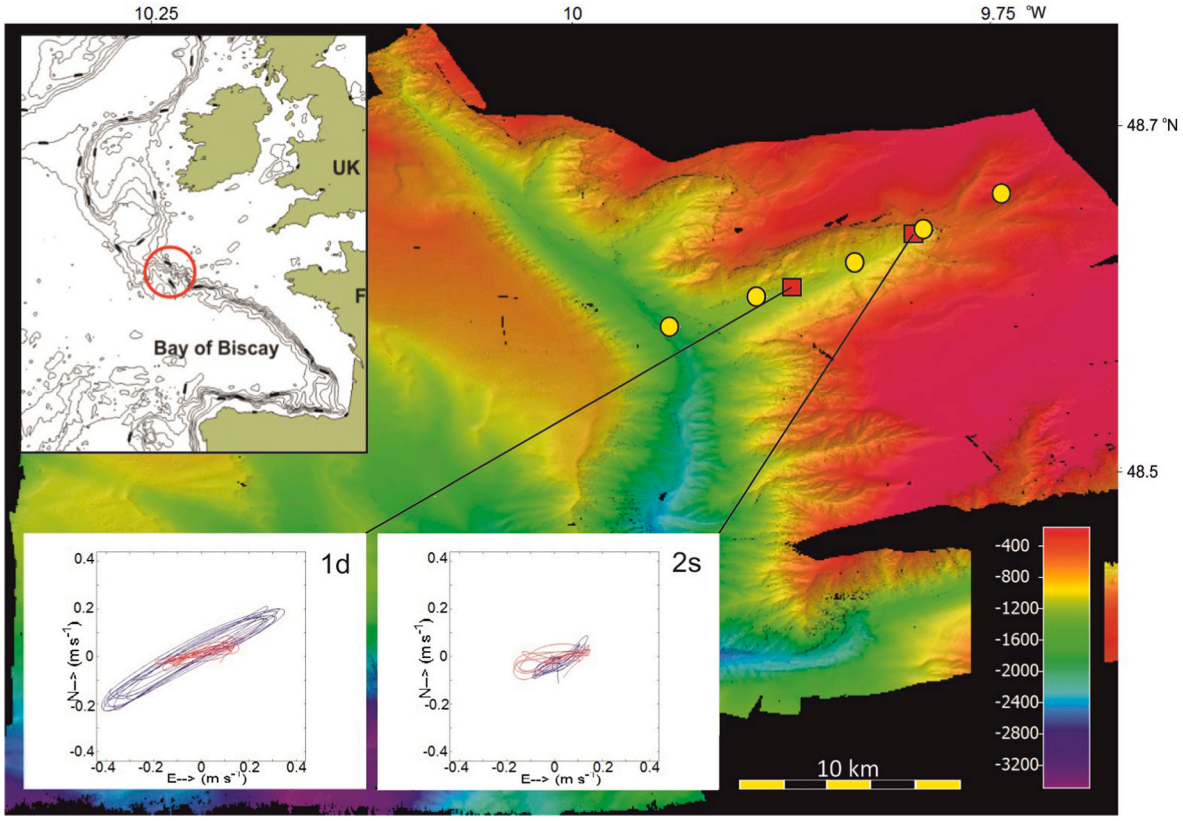

Fig. 1. Multibeam map of the easternmost branch of Whittard canyon, with CTD (yellow dots) and mooring (red squares) locations (1d(eep) and 2s(hallow)) in the tributary and water-flow current ellipses from tidally band-pass filtered ADCP data with cut-offs at 0.6 and 6 cpd (cycles per day) from about 30 m (blue) and 280 m (red) above the local seafloor. The ADCP compass data are corrected for the local declination.

(Fig. 2d).

Turbulence values are obtained using the moored T-sensor data by calculating 'overturning' scales. These scales follow after reordering every 1 s the 240 m high potential density (conservative temperature) profile $\sigma_1(z)$, which may contain inversions, into a stable monotonic profile $\sigma_1(z_s)$ without inversions (Thorpe, 1977). After comparing observed and reordered profiles, displacements $d = \min(|z\text{-}z_s|)\cdot\mathrm{sgn}(z\text{-}z_s)$ are calculated necessary for generating the reordered stable profile. Certain tests apply to disregard apparent displacements associated with instrumental noise and post-calibration errors (Galbraith and Kelley, 1996). Such a test-threshold is very low for NIOZ-temperature sensor data, $<5 \times 10^{-4}$°C (van Haren, 2018). Then, using d rather than its rout-mean-square rms value as explained in the paragraph below,

$$\varepsilon = 0.64 d^2 N^3, \quad (3)$$

the turbulence dissipation rate, where N denotes the buoyancy frequency computed from each of the reordered, essentially statically stable, vertical density profiles. The numerical constant follows from empirically relating the root-mean-square 'rms' overturning scale with the Ozmidov-scale of largest isotropic turbulence overturns in a stratified fluid $L_O = 0.8 d_{rms}$ (Dillon, 1982).

In (3) we use individual d to replace overturning scales, rather than taking their rms-value across a single overturn as originally proposed by Thorpe (1977). The reason is that we cannot easily distinguish individual overturns, first, because overturns are found at various scales with small ones overprinting larger overturns, precisely as one expects from turbulence, and, second, because some exceed the range of temperature sensors. Instead, we first calculate non-averaged d in (3) for high-resolution time-depth images of $\varepsilon(t, z)$. Subsequently, we calculate 'mean' turbulence values by arithmetic averaging in the vertical [ ] or in time <>, or both. (This yields average values which are about a factor of 2 lower than if we would use the rms-value of d, commonly defined as 'Thorpe-scale', and mean N, both arithmetic operations over the entire vertical range, in (3).) Arithmetic averaging is mandatory over the vertical overturning scales to represent proper turbulence dissipation rates. Although turbulence dissipation rates are not normally distributed, arithmetic averaging is also used for time averaging, for consistency. Geometric time averaging following arithmetic vertical averaging would provide a factor of 1.5–2 lower mean values than presented in this paper. We note that this discrepancy is still within the error range, see next paragraph. The small discrepancy between geometric and arithmetic time averaged values may be because ocean turbulence temperature variance and dissipation rate are not necessarily log-normally distributed due to intermittency and multiple nonlinear sources (Cimatoribus and van Haren, 2015; Cael and Mashayek, 2021). The 1-Hz sampling of moored T-sensor profile data allows sufficient averaging over all different turbulence characteristics.

The errors in the mean turbulence values thus obtained depend on the error in N, the error in the temperature-density relationship while the instrumental noise error of the thermistors is negligible. Given the errors, the estimated uncertainty in time-depth mean estimates of dissipation rate amounts about a factor of two, which is the minimum error range for turbulence values (Oakey, 1982). It is presently impossible to try better in natural waters where turbulence values from individual overturns vary over four orders of magnitude (e.g., Oakey, 1982; van Haren and Gostiaux, 2012; Gregg et al., 2018). Using similar T-sensor data from Great Meteor Seamount, van Haren and Gostiaux (2012) found turbulence values to within a factor of three similar to those inferred from ship-borne CTD/LADCP profiler data using a shear/strain parameterisation near the seafloor. Their values comply well with profiler-based estimates in similar sloping topography areas by Klymak et al. (2008). It has been argued that L_O/d_{rms} varies as a function

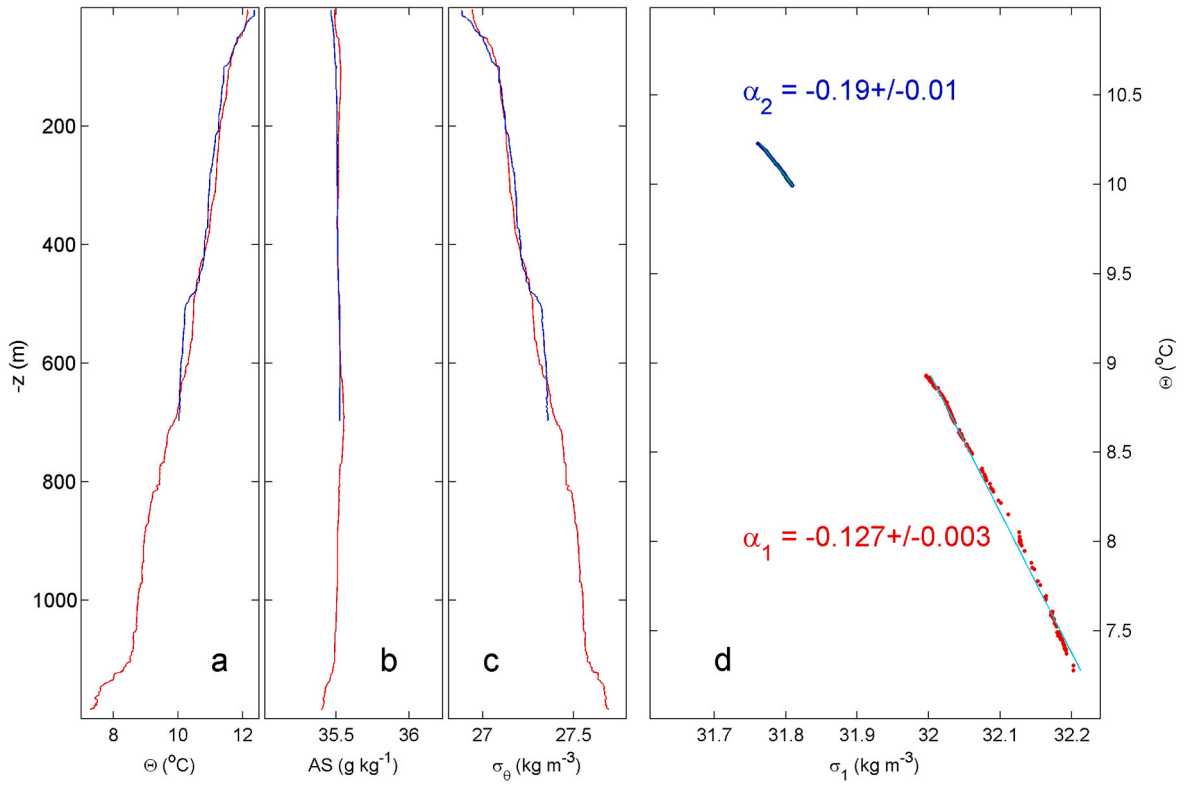

Fig. 2. Shipborne CTD-observations down to 5 m above the seafloor to within 1 km horizontally from the moorings 1d in black and 2s in red. (a) Conservative Temperature. (b) Absolute Salinity, with the x-axis range approximately the same as in a. in terms of density variations. (c) Density anomaly referenced to the surface. (d) Conservative Temperature-density anomaly (referenced to 1000 dbar) relationships, from the lower 300 m of CTD-profiles, with best-fit lines in light-blue and green, respectively.

of stratification, stage and type of turbulence generation (e.g., Chalamalla and Sarkar, 2015; Mater et al., 2015). While this is acknowledged for specific unique conditions like pure convection and/or low Reynolds number flows, there are several reasons why it may not apply, and cannot be applied, to the present ocean data, as partially outlined in van Haren (2017) and summarized hereafter.

The moored high-resolution T-sensor data provide every second a 240 m tall profile of temperature and thereby a priori insight in particular internal wave turbulence processes. However, we are not primarily concerned with individual overturning values. Instead we give "suitably averaged" turbulence values, as detailed below. In any given high Reynolds number environment like the deep ocean, shear- and buoyancy(convection)-driven turbulence intermingle and are hard if not impossible to separate. Examples of numerical modelling studies of particular stages of instability developments show that a finger of convective instability develops secondary shear instability along its fringes (Li and Li, 2006), while the roll-up stage of shear instability develops secondary convective instability mushrooms (Matsumoto and Hoshino, 2004). Comparison between calculated turbulence values using shear measurements and using Thorpe overturning scales with $L_O/d_{rms} = 0.8$ from areas with such mixtures of turbulence development above sloping ocean topography led to 'consistent results' (Nash et al., 2007). Thus, from the argumentation above and the reasoning in Mater et al. (2015), internal wave breaking unlikely biases turbulence dissipation rates computed from Thorpe overturning scales by more than a factor of two to three, provided some suitable time-space averaging is done instead of considering single profiles. This is within the range of our error.

3. Observations

The two moorings were deployed and recovered in the tributary of Whittard Canyon during the short 8-day cruise with the R/V Pelagia (cruise 64PE437). In this paper we discuss the two days of time-overlapping data when the moorings were simultaneously collecting data. Although Conservative Temperature is presented and used throughout, we will henceforth refer to it as 'temperature' in the text.

3.1. Average profiles

The first and second moments of statistical probability function of temperature and along-canyon current component show considerable differences for the two moorings which were only 6.5 km apart horizontally and 340 m vertically (Fig. 3a and b). The shallower mooring 2s demonstrates temperature and current vertical variations of which the time-mean values (current only) and standard deviations are more constant in the vertical over the range between 7 and 247 m above the seafloor than at the deeper mooring 1d. While temperature variations show a maximum between about 60 and 80 m above the seafloor in both moorings (Fig. 3a), the 2s-mooring shows considerable smaller and vertically near-constant current changes (Fig. 3b). At mooring 1d, the mean along-tributary current varies from upslope to downslope while its standard deviation increases monotonically towards the seafloor. The cross-tributary current component has considerably smaller amplitudes (Fig. 1). Likewise, the time-mean dissipation rates are vertically near-homogeneous at 2s, while monotonically increasing over one order of magnitude towards the seafloor at 1d (Fig. 3c). However, the two-day time and 240-m vertical mean values are statistically indistinguishably identical for both moorings: $[<\varepsilon_1>] = 4.41 \pm 2 \times 10^{-7}$ m^{2}s^{-3}, $[<\varepsilon_2>] = 4.44 \pm 2 \times 10^{-7}$ m^{2}s^{-3} (the insignificant digits are kept to demonstrate the small difference between the values). This mean turbulence dissipation rate is found in stratified waters with almost identical mean buoyancy frequencies from reordered profiles: $[<N_1>] = 3.1 \pm 0.3 \times 10^{-3}$ s^{-1} for mooring 1d and $[<N_2>] = 3.0 \pm 0.3 \times 10^{-3}$ s^{-1} for mooring

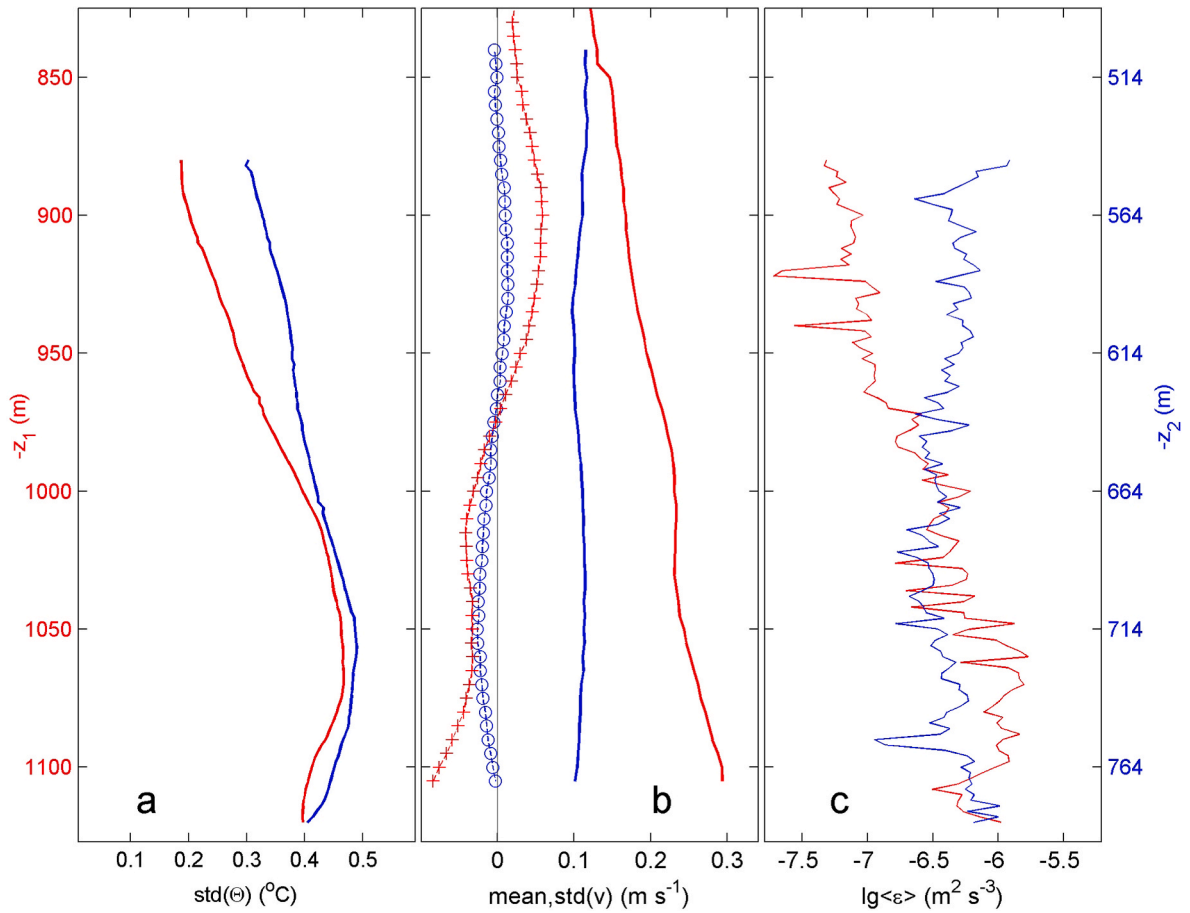

Fig. 3. Vertical profiles of time-mean characteristics from two days of simultaneous mooring data from 1d (red) and 2s (blue, vertical scale to right). The y-axes are shifted to present data with respect to the local seafloor. (a) Standard deviation of Conservative Temperature variations from T-sensor data. (b) Mean values (+and o, respectively) and standard deviation (solid lines) of along-tributary current component from ADCP-data. (c) Logarithm of time-averaged dissipation rate from T-sensor data.

2s, or mean buoyancy periods $T_N = 2\pi/N$ of about 2050 s. Although large-scale mean buoyancy frequencies vary somewhat on the long term, the average semidiurnal internal tidal slope angle for propagating waves is $1.7 \pm 0.2°$. This angle is close, 'critical', to the bottom slope angle in along-tributary direction at the deep site. It is significantly smaller than all other 'supercritical' side-canyon slopes.

As will become clear from the time series below, the dominant variations with time have a semidiurnal tidal periodicity. The tidally band-pass filtered current ellipses are more or less directed East-West and have about the same amplitude at about 280 m above the seafloor at both moorings (Fig. 1). Closer to the seafloor, presumably a topographic correction forces the more or less rectilinear tidal flow in the direction of the tributary axis, with a strong amplitude increase at the deep site only.

3.2. Time series

With reference to the ADCP's pressure (p) sensor, the taut-wire moorings did not move more than about ±0.1 m vertically due to mooring drag. This was anticipated given the current magnitudes <0.3 m s^{-1} and the large floats used. The observed pressure variations are mainly due to surface elevations, which are dominated by a barotropic semidiurnal tide (Fig. 4a). Time series of temperature variations in both the upper 2s and lower 1d T-sensors in the deep ocean interior are also dominated by semidiurnal variations (Fig. 4b), but these variations are out-of-phase with the surface tidal pressure variations by approximately 100°. The temperature variations are also considerably deformed from a sinusoidal signal like the pressure record, i.e. they are strongly nonlinear, more resembling a saw-tooth signal with a long increase and short drop in temperature (upper 2s and lower 1d), a triangular (lower 2s) or a block (upper 1d) signal. The lower 2s signal demonstrates a relatively strong higher tidal harmonic signal, notably fourth-diurnal. The lower 1d signal shows relatively strong high-frequency temperature variations occurring approximately half-way the long increase in temperature. Vertically, the tidal cooling phase starts near the seafloor compared with higher-up at 2s, and the opposite (higher-up before the seafloor, at 1d (Fig. 4b). In complete order, cooler phase waters pass at upper-1d T-sensor, then lower-1d, upper-1d and lower-2s.

The 80-m vertically averaged dissipation rate time series, low-pass filtered with cut-off at 20 cpd (cycles per day) ≈ 0.5N, demonstrate only partial correspondence with the semidiurnal signals (Fig. 4c). Most agreement with a semidiurnal signal shows the upper 1d record, which has smallest turbulence dissipation rate, and which corresponds in time series variation with the lower 1d temperature record (Fig. 4b). On average more equal dissipation rates are observed in the other three records that nonetheless vary over 1.5 orders of magnitude with time and without clear dominance of semidiurnal or fourth diurnal signals, except perhaps in the second part of the upper 2s record (semidiurnal). The lower 1d record generally shows highest peaks during a tidal period, which occur during the time of sharp temperature decreases and in a double fashion of two peaks about 2h apart of which the second one is the highest in all three cases. More high peaks in the lower 1d record associate with the high-frequency temperature variations during the warming phase in a tidal period. Then also a peak in lower 2s dissipation rate record is observed.

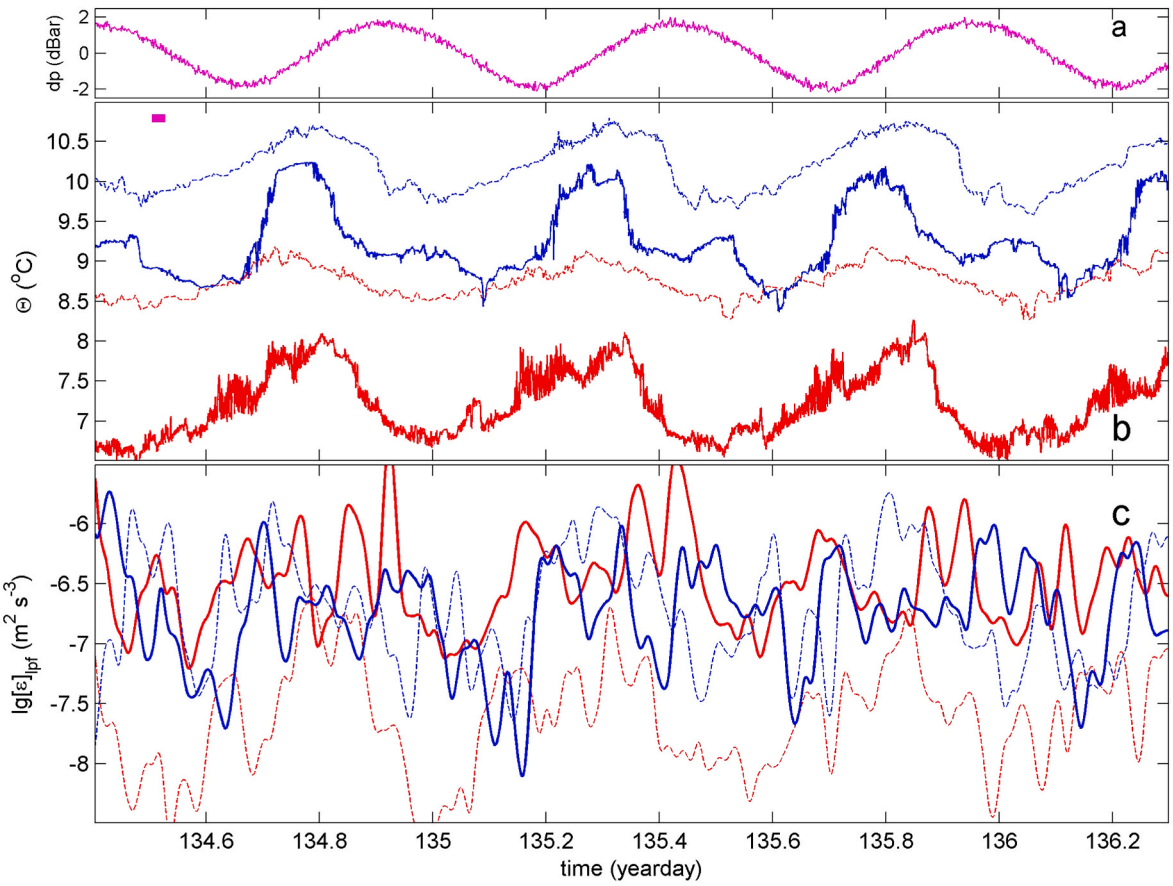

Fig. 4. Time series of characteristics from two days of simultaneous mooring T-sensor data from moorings 1d (red) and 2s (blue). (a) Pressure relative to its mean value from ADCP at 1d. Similar data from 2s are in phase and indistinguishable. (b) Conservative Temperature from the 10th (dashed) and 110th (solid) T-sensors in each mooring. The purple bar indicates the mean buoyancy period. (c) Logarithm of 3-h low-pass filtered dissipation rate from T-sensor data vertically averaged over 80 m from upper (dashed) and lower (solid) ranges of each mooring.

3.3. Time-depth series

An overview of the two-day, 240-m time-depth series of temperature demonstrates the clear domination by the internal tide in the signals at the two mooring sites (Fig. 5). Isotherms make vertical excursions with time suggesting wave heights of more than 200 m (crest-to-trough) at mooring 2s and over about 150 m at mooring 1d. This is 40 to over 50 times larger than the surface tidal range (Figs. 4a and 5). While the surface tidal (pressure) signals are undistinguishably identical at the two sites, the internal tide (isotherm-excursion) signals have a different appearance between the two sites (Fig. 5). The different appearance occurs every semidiurnal period, with small changes between these periods. Although the internal tidal isotherm excursions have a large phase difference with the surface tidal elevations, they are approximately in-phase between the two moorings along the (sub-)canyon.

At the shallow site, the largest isotherm excursions occur in the relatively warmer waters higher-up in the range of observations (Fig. 5a). While the plotted temperature range is 2.8 °C, in both panels of Fig. 5, the larger upper layer excursions cause the isotherms to become more densely packed in the lower layer, especially during downward warming and upward cooling phases (Fig. 5a). Over hundred meter thick near-homogeneous layers are found between about $-750 < z < -600$ m, during the warm phase of each semidiurnal period, e.g., on day 134.78, and the first cooling maximum or cold front, e.g., on day 134.93. A secondary cold front is typical for the lower half of Fig. 5a following a downdraught of relatively warm water from above that reflects the fourth-diurnal temperature signal.

At the deep site, no clear distinction is observed in the internal tidal wave isotherm displacements between lower and upper half of the range of observations in Fig. 5b. Isotherms approximately maintain their distance throughout a semidiurnal cycle, and thus do not strain as much as at mooring 2s in Fig. 5a. They do show much more high-frequency variations and are less smooth, especially in the lower $-1100 < z < -1050$ m towards the end of the warming phase, e.g., days 134.6–134.75. The single cold front initiating the cooling phase, e.g., on day 134.85, is considerably sharper than in Fig. 5a but it occurs on average 1 h later in time near the seafloor. The sharp front extends up to about 100 m above the seafloor and forces upward displacement of isotherms throughout the range of observations. This contrasts with the less intense frontal passage in Fig. 5a, which is associated with partial continued warming in the upper layer above the cooling passing near the seafloor. Nevertheless, judging from both the moment of maximum warming and the passage of 1 °C cooler water near the seafloor, these observables occur about 1 h earlier at the shallow site than at the deep site (cf., Fig. 4b).

The associated time-depth distribution of (non-averaged) turbulence dissipation rate (Fig. 6) shows even more contrast between the two sites than the temperature time-depth distribution.

At the shallow site, higher turbulence dissipation rate is found throughout the vertical, but in different patches of about 100 m tall at different times across different vertical ranges (Fig. 6a). The above mentioned near-homogeneous layers associate with enhanced dissipation, as do the warm downdraughts in the upper layers. Near the seafloor, higher dissipation is found in smaller portions notably occurring every end of a warming phase when packed isotherms touch the seafloor. During the first cold phase of each semidiurnal period an about

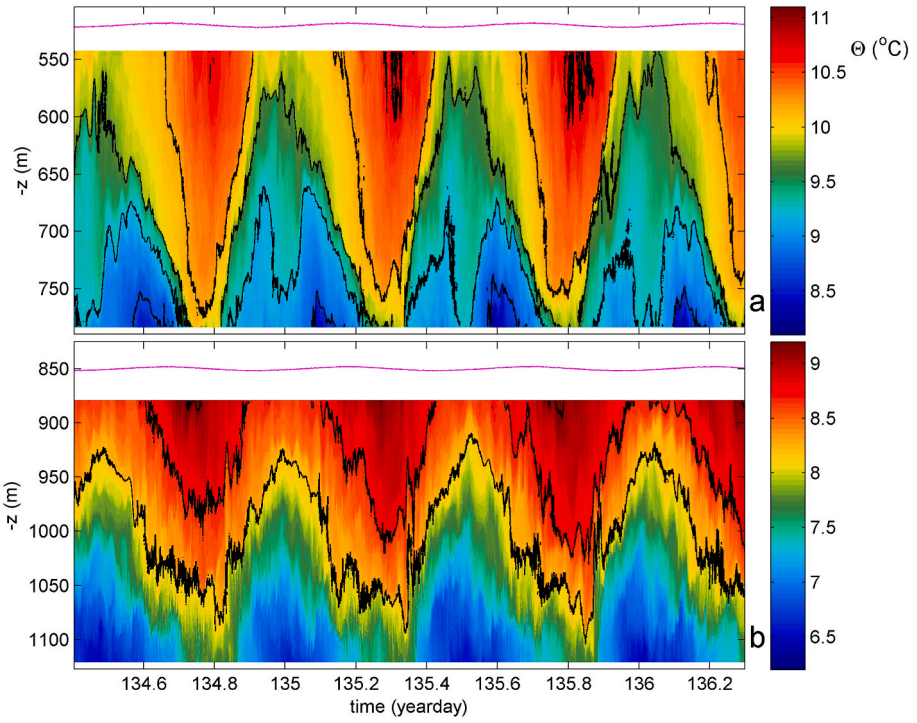

Fig. 5. Simultaneous time-depth series of Conservative Temperature with black contours every 0.5 °C. The purple graphs indicate pressure at the ADCP shifted vertically by about 50 m. (a) Mooring 2s, with data from 10 T-sensors linearly interpolated between neighbouring sensors. The horizontal axis is at the local seafloor. (b) As (a), but for mooring 1d with data from 9 T-sensors interpolated.

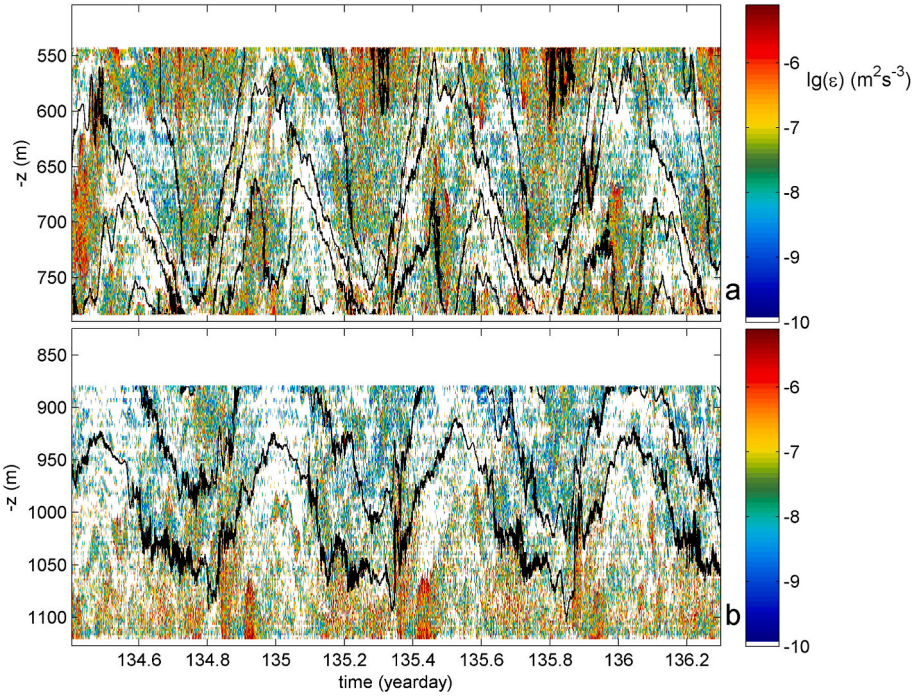

Fig. 6. As Fig. 5 including the black contours every 0.5 °C, but for (non-averaged) turbulence dissipation rate. Colour ranges and scales are identical in a. and b.

100 m thick near-homogeneous layer passes that episodically reaches to the seafloor. Cold fronts occasionally show large dissipation, in the present record only on day 135.33.

At the deep site, strong dissipation reaches to the seafloor during the passage of all cold fronts (Fig. 6b). The largest >50 m tall but least intense dissipation peak is at the first front followed by a more intense and smaller ~50 m tall patch passing with a second front about 2 h later. The seafloor is also reached by moderate dissipation under every warming phase when the high-frequency isotherms excursions are observed and where stratification is not particularly weak. In the upper layer, turbulence dissipation is much less intense and its rates contrast with the larger dissipation rate values observed near the seafloor.

To investigate if large dissipation rates associate with large relative acoustic echo intensity that may reflect suspended matter, we compare

Fig. 6 with Fig. 7 and investigate episodes with high turbulence levels. The association is known to hold for frontal bores, one per tidal period, moving upslope over and touching the seafloor whereby sediment is resuspended (Hosegood et al., 2004). This is observed here too, but at the deep site only (Fig. 7b) and for more than one peak in dissipation rate near the seafloor per semidiurnal period. It is noted that the dissipation peak associated with the second front shows less correspondence in echo intensity. Two further observations are noticed in the present data.

At the shallow site, largest echo intensity is associated with temperature between 10 and 10.5 °C and corresponds with the large dissipation observed during the downward warm water from above (Fig. 7a). As far as can be observed, high echo intensity reaches (near) the seafloor from above, and never reaches upward from below.

At the deep site, higher echo intensity reaches not only upward from the seafloor during cold-phase frontal bore passages, but also episodically during the 4 h before under the high-frequency internal motions under the warm phase from above (Fig. 7b). There is no association with material being pushed downward by the warmer waters above, as we observe a layer of weaker echo intensity between the intermediate isotherms of 8.0 and 8.5 °C. Nonetheless, the entire upper layer shows enhanced echo intensity for temperature >8.5 °C, although having lower values than observed at the shallow site. It is noted that the quasi-permanent high echo intensity levels exceeding noise levels in this upper layer somewhat complicate the correction method for sound attenuation in water proposed by Gostiaux and van Haren (2010), cf. Appendix A. A difference in the amount of suspended matter in the water column was observed in the (limited) CTD transect along the axis of the tributary (Fig. 8), in which the shallower part showed relatively low turbidity values compared to the deeper part, pointing to enhanced particle load at depth as was also observed in the moored ADCP data (Fig. 7). As we use single acoustic frequency instrumentation, direct comparison of echo intensity with suspended matter content is difficult and we are reluctant to infer quantitative results on sediment transport.

The upper layer higher echo intensity during the warming phase is not associated with particular along-canyon v-current component (Fig. 9). During its passage, the v-component is directed down-canyon, partially, before turning up-canyon.

At the shallow site of mooring 2s, an upward, positive vertical phase propagation of 2.5–3 h is observed in positive maximum v and about 6 h in the transition between positive to negative v, over the 240 m vertical range of observations (Fig. 9a). In the lower 50 m near the seafloor a distinct small positive-v pulse is associated with the secondary cold-'front' passing 5–6 h after start of the large positive v-pulse. This provides a fourth-diurnal harmonic in v. Recall that positive-v is directed up-canyon (Fig. 1).

At the deep site of mooring 1d, the single vertically uniform transition from negative to positive, down-to up-canyon, v-component is associated with the steep front in isotherms leading the up-canyon propagation of the cold water phase (Fig. 9b). The preceding high-frequency internal motions are associated with down-canyon v when its speed values are >0.3 m s^{-1} near the seafloor.

3.4. Frequency distributions

The large number of T-sensors provide opportunity to improve scalar temperature statistics even though the time series length is limited. We separated the records from both moorings in two parts, the upper 100 m and the lower 100 m of the 240 m vertical ranges. Average temperature variance spectra were computed (Fig. 10a,c) as well as coherence over 2 and 10 m vertical distances between all possible pairs of independent T-sensors (Fig. 10b,d). The comparison between the shallow site (Fig. 10a and b) and deep site (Fig. 10c and d) supports some of the time series observations and adds new information especially when focusing on the super-buoyancy frequencies that contain a transition from stratified anisotropic to isotropic turbulence.

At the shallow site, very similar shapes of temperature variance are found in upper and lower layers, but the level of variance is about half an order of magnitude larger for the lower layer, except at the semidiurnal frequency (Fig. 9a). Outside the tidal and inertial harmonic frequencies $\sigma > M_4$, fourth diurnal lunar frequency, the turbulence inertial subrange $\sigma^{-5/3}$ scaled spectra (Tennekes and Lumley, 1972) slope −1/3 in the

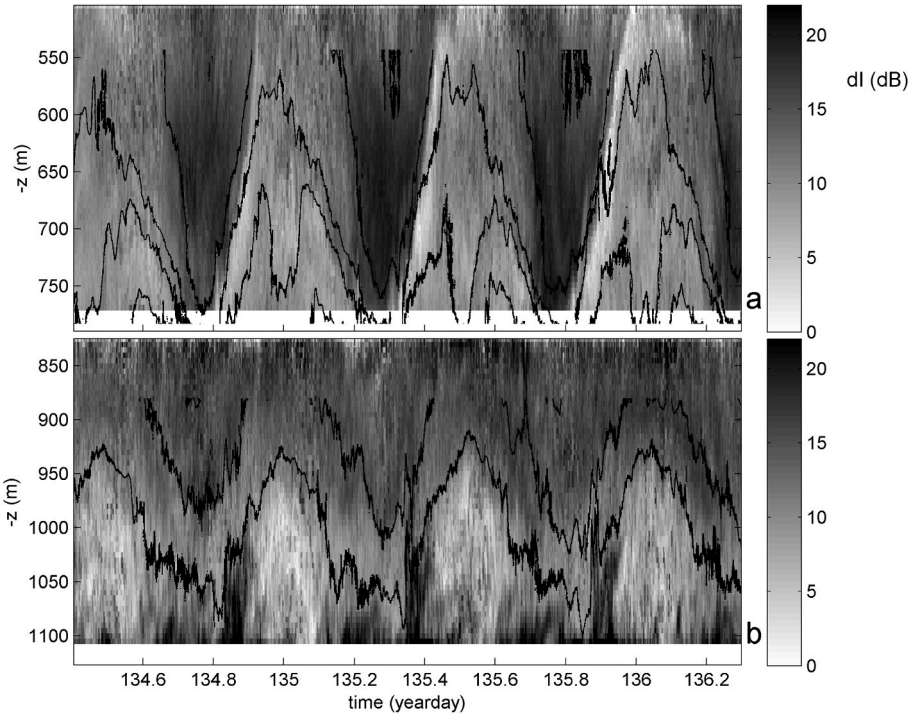

Fig. 7. As Fig. 6, but for ADCP's relative echo intensity corrected for water attenuation and noise level of sound following Gostiaux and van Haren (2010), see Appendix A.

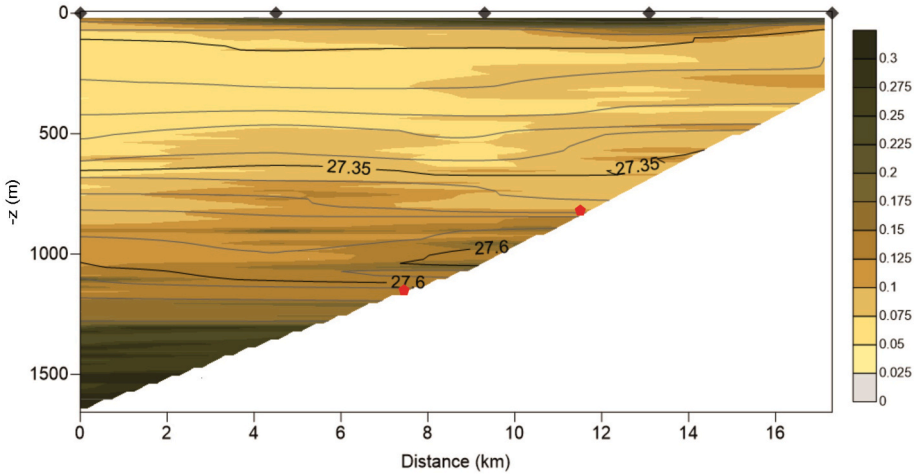

Fig. 8. Z,x map of turbidity in colours (NTU) and density anomaly σ_θ in black contours (kg m^{-3}) from CTD transect made along-tributary between days 135.6 and 135.8. The five diamonds on top indicate the relative station positions. The two red dots on the sloping seafloor indicate the relative mooring sites.

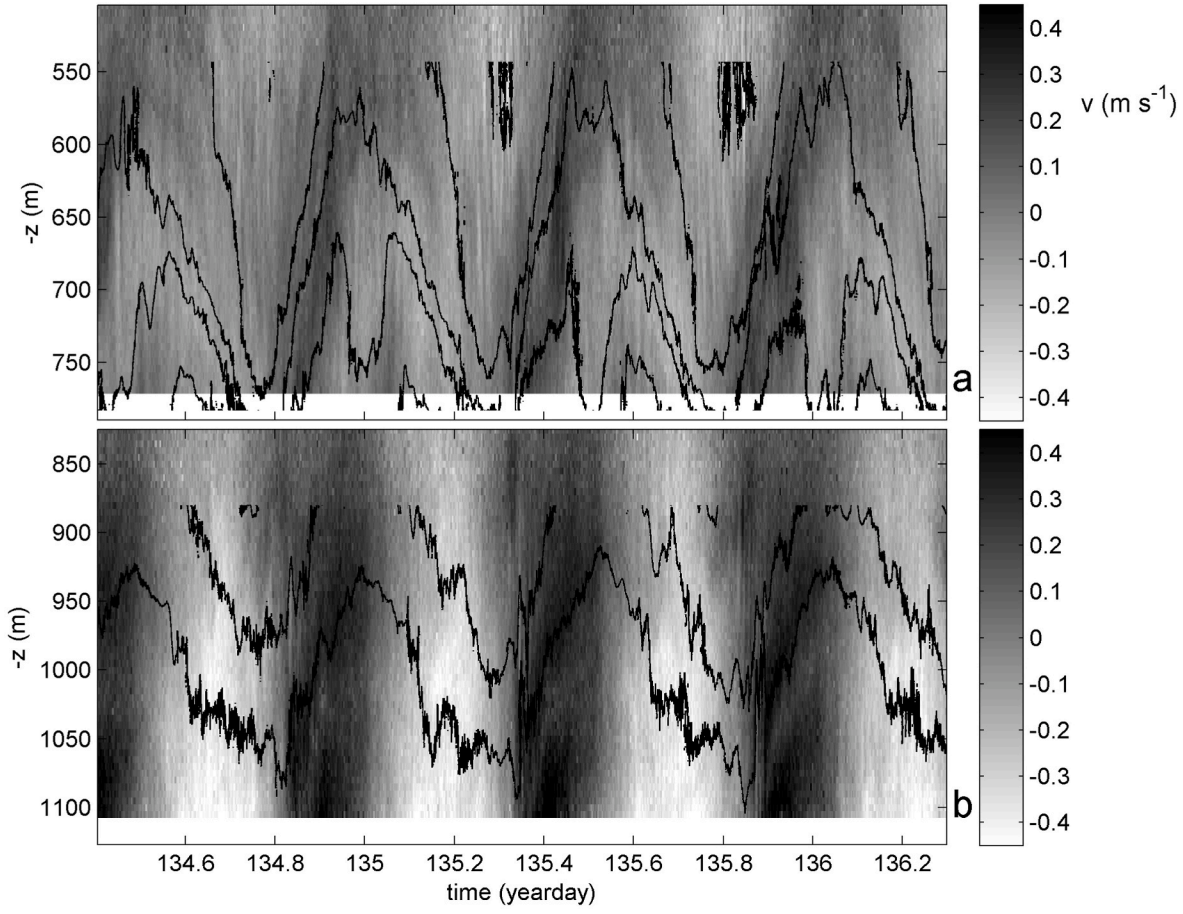

Fig. 9. As Fig. 6, but for ADCP's along-canyon current component.

log-log plot, which is a slope of −2 in unscaled log-log plotting. This σ^{-2} is the canonical internal wave slope (Garrett and Munk, 1972), which is normally considered for freely propagating internal waves in the range f $< \sigma <$ N while internal tides are not included in the model description. Here, the slope extends between (f <) $M_4 < \sigma < N_{s,max} \approx \sigma_O$, where $N_{s,max}$ denotes the maximum small-2-m-scale buoyancy frequency in thin layers in the record ranges and σ_O the Ozmidov frequency that separates the buoyancy range of stratified anisotropic quasi-2D turbulence at $\sigma <$ σ_O, and the inertial subrange of isotropic 3D turbulence at $\sigma > \sigma_O$. We compute the Ozmidov frequency using the mean current flow speed observed by ADCP in both upper and lower layers. Indeed, a kink is observed in spectral slope to 0 (i.e. −5/3 of inertial subrange in unscaled log-log plotting) near σ_O for both layers. At the Ozmidov frequency, the coherence at 2-m intervals is approximately 0.5 ± 0.05, with slightly larger values for the upper layer, while the coherence at 10 m vertical intervals drops into noise levels, equal for both layers. At large-scale

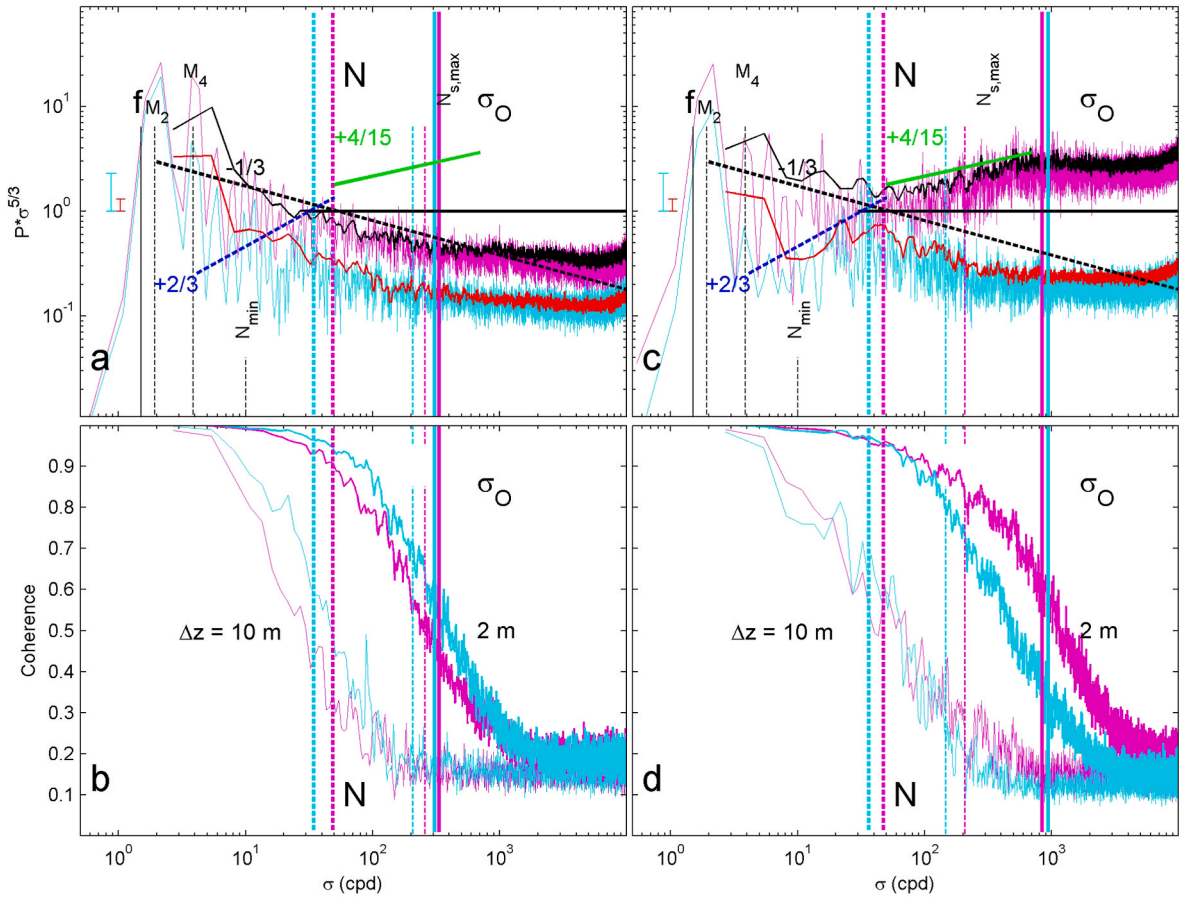

Fig. 10. Spectra for lower and upper 100 m (purple/black and light-blue/red, respectively) of T-sensor data. (a) Log-log plot of temperature variance from mooring 2s scaled with the inertial subrange slope −5/3 (horizontal black line) in nearly raw (10 degrees of freedom 'dof'; thin-line graphs) and moderately smoothed (50 dof; thick-line graphs) forms. Vertical colour lines indicate the associated mean large-scale N and maximum small-scale $N_{s,max}$ buoyancy as well as the Ozmidov frequencies σ_O. Vertical black lines indicate the minimum buoyancy frequency N_{min}, tidal M_2, M_4, and inertial f frequencies. The sloping lines indicate several deviations from the inertial subrange (see text). (b) Coherence between all possible pairs of 2-m (thick-line graphs) and 10-m (thin-line graphs) separated T-sensors from mooring 2s. (c) As a., but from mooring 1d. All slopes are identical as in a., for reference, but vertical lines show locally calculated values (except for M_2, M_4). (d) As b., but from mooring 1d.

mean buoyancy frequency N, 2-m interval coherence values are >0.9, while 10-m interval coherence values are about 0.5.

At the deep site, the upper layer temperature variance is approximately the same in level (slightly larger) and shape as at the shallow site, except for a variance-dip in the internal wave band for $M_4 \leq \sigma < 0.5N$ (Fig. 10c). This dip may associate with a slope of +2/3 (or −1 in an unscaled log-log plot) for open-ocean internal waves far from boundaries (van Haren and Gostiaux, 2009). It includes less internal tide nonlinearity as the fourth diurnal tidal harmonic is rather weak. In the lower layer, the fourth diurnal frequency is less weak in variance, although still an order of magnitude smaller than in the lower layer at the shallow site, but for $\sigma > 0.5N$ variance is larger at the deep site up to more than one order of magnitude at $\sigma > \sigma_O$. For the buoyancy-Ozmidov frequency band $N < \sigma < \sigma_O$ the lower layer deep site spectrum slopes at +4/15, which is −7/5 in an unscaled log-log plot. This significant deviation from the inertial subrange $\sigma^{-5/3}$ scaling points at convective turbulent overturning of an active scalar (Pawar and Arakeri, 2016; van Haren and Dijkstra, 2021), and which is separated at σ_O from the inertial subrange slope for an environment with dominant shear-induced turbulent overturning of a passive scalar (Warhaft, 2000). Its spectral variation is about 1.5 times rougher than would be expected for (random) statistical spectral noise variation as observed for the inertial subrange at $\sigma > \sigma_O$. This rougher, less smooth spectral slope corresponds with similar findings for shear-dominated strong intermittent internal wave breaking above an open ocean slope in the same range that is also attributed to anisotropic 'stratified' turbulence (van Haren, 2019). At the deep site, the frequencies of σ_O and $N_{s,max}$ do not coincide, which may have to do with unresolved small-scale motions. However, the temperature variance demonstrates that for the upper layer the internal wave slope transits at $N_{s,max}$ to the inertial subrange slope. The corresponding 2-m coherence is larger in the lower layer than in the upper layer and at the shallow site. For both sites, upper layer coherence shows approximately the same coherence plot, with slightly different Ozmidov frequency, while the 10-m coherence is reached at $\sigma_O/N_{s,max}$ for both layers.

3.5. Convection and shear details

The spectral information is an average over the two-day time series and 100 m vertical sections. Within those time-depth intervals stratification, internal wave and turbulence properties vary considerably. For example, the minimum buoyancy frequency in weakly stratified layers reaches down to $N_{min} = 0.25 \pm 0.05N$, about 10 cpd (compare with an open ocean minimum value of about 5 cpd (van Haren and Gostiaux, 2009), thereby smearing the boundaries of the transition between internal waves and stratified turbulence. The frequency information thus represents average information that may be dominated by a particular process for the time-depth interval. Here we seek to clarify the observed difference between lower layer convective and shear induced turbulence, that resulted in the difference in lower-layer spectral slopes in

Fig. 10a,c between the two sites.

In detail plots of 2.3-h duration, which is just longer than the minimum buoyancy period of about 8000 s, and depicting the lower 110 m above the seafloor, we highlight two phenomena that are essentially different between the two sites and occur every tidal period. In Fig. 11, we focus on the end of the warming phase. In Fig. 12, we show the turbulence around 2 h after the passage of the front starting the cooling phase.

In both Figs. 11 and 12, the shallow site turbulent overturning shows many time-length scales that generally are associated with shear-induced turbulence. The warming phase is more stratified near the seafloor and thus characterized by smaller scales (Fig. 11a) than the cooling phase (Fig. 12a). The deep site shows turbulent overturning that is more vertically oriented in tall short-timescale up- and down-going motions that are associated with convective turbulence. While the vertical excursions have roughly the same time-depth scales between the two periods, the warming phase shows convection in stably stratified waters throughout Fig. 11b, whereas the cooling phase convection is initially occurring in unstable waters in which relatively cooler water is moved over warmer, less dense water (Fig. 12b). After about 1.5 h, one local (minimum) buoyancy period, the convection occurs in stably stratified waters as during the warming phase.

While convection is best understood to occur under unstable conditions of warmer water under cooler water as driven by gravity, here possibly initiated by the advecting up-canyon flow when it peaks just after the front at some distance above the seafloor whereby denser water from deeper down the canyon is driven over less dense water from higher-up, the convection under stable conditions ('stratified convection') is suggested to be driven by internal waves overcoming reduced (density-difference driven) gravity (van Haren, 2015). Although in the ocean salinity may contribute to density variations even though the temperature-density relationship seems tight as at the present site (Fig. 2d), stratified convection has also been observed under internal waves in a fresh-water lake (van Haren and Dijkstra, 2021). We note that the present cooling phase stratified convection occurs when the isotherms bend downward, so no longer move upward as during the start of the cooling phase. In both phases, convection occurs during most intense tidal along-canyon flow, whether down-canyon (warming phase) or up-canyon (cooling phase). Near-bottom intensified tidal flow is not observed at the shallow site.

4. Discussion and conclusions

The 240-m vertical and two-day time mean turbulence dissipation rates are highly comparable between the two sites, to within one standard deviation or well less than a factor of two. The mean values are of the same order of magnitude as values found under breaking internal waves above deep-sea sloping topography where freely propagating semidiurnal internal tides dominate (van Haren and Gostiaux, 2012; van Haren, 2019). Our values are also highly comparable with those observed just shelf-ward of the East Atlantic shelf-break where very energetic tides are found on the relatively shallow Celtic Shelf (Palmer et al., 2015; Inall et al., 2021).

In detail however, over distances as short as 6.5 km, we find considerable large differences between our two observational sites in internal wave breaking processes and turbulence episodes near the seafloor. The deep site shows most resemblance with internal tide sloshing against more open large-scale two-dimensional topography like a large seamount (e.g., low-resolution data in Aucan et al., 2006; high-resolution data in van Haren and Gostiaux, 2012). Per tidal period, two or three peaks in vertically averaged turbulence dissipation rate are observed in the tributary, of which the largest occurs during the passage of the warming to cooling phase upslope propagating front. The secondary front observed at the deep site in the canyon 2 h later during maximum upslope flow, which was also observed above Great Meteor Seamount (van Haren and Gostiaux, 2012), associates with weaker stratified waters and weaker acoustic echo intensity, although turbulence overturning reaches the seafloor. The third large turbulence episode at 1d, which was not clearly observed in van Haren and Gostiaux (2012), reaches the seafloor during the (maximum) warming down-going phase. At the deep site in the tributary this turbulence has a distinct convective character, which contrasts with dominant shear-induced turbulence during the passages of the frontal bores.

Spectrally, the convection is found in the band between the buoyancy and Ozmidov frequencies, when internal waves transit to anisotropic stratified turbulence. The convection extends coherence over 2-m

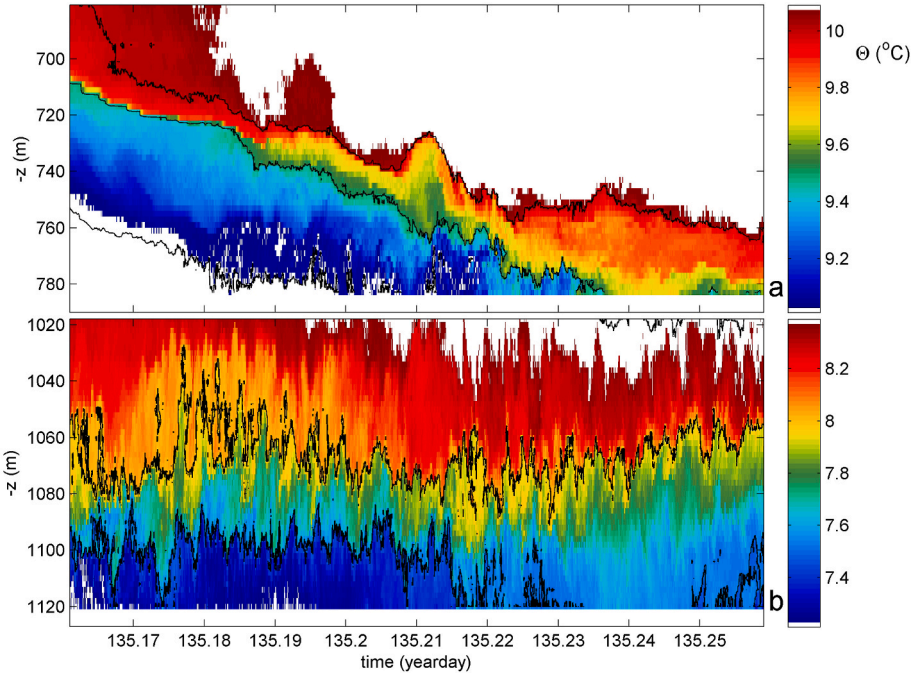

Fig. 11. 2.3 h, lower 110 m detail of Fig. 5, with different colour scales, demonstrating convective turbulent overturning near the seafloor at the deep site only during the down-canyon warming phase.

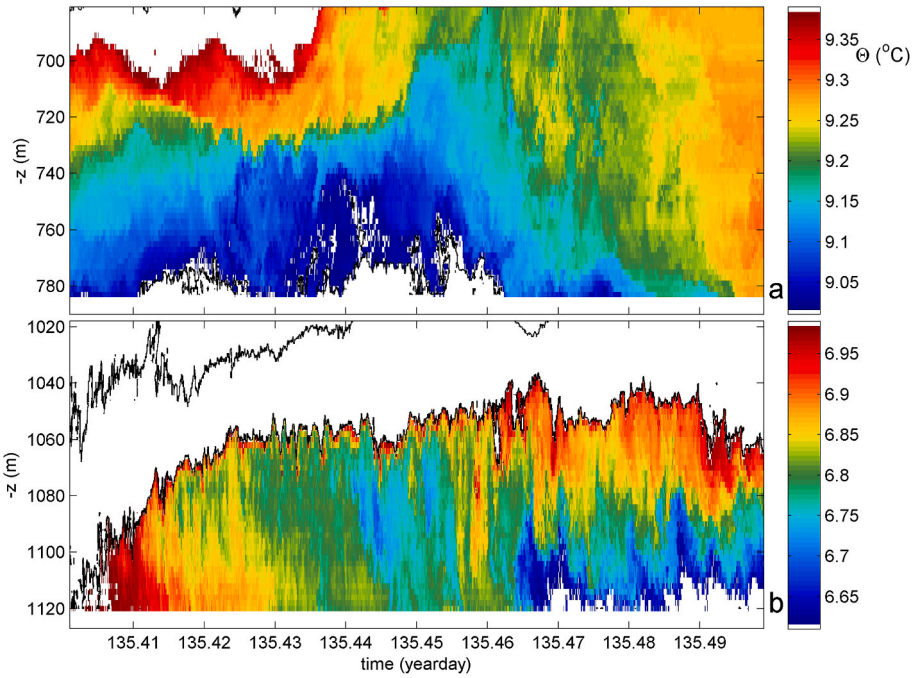

Fig. 12. As Fig. 11, with different colour scales, but during the up-canyon cooling phase about 2 h after the passage of a first near-bottom front.

vertical scales to higher frequencies by at least half an order of magnitude. At the transition from anisotropic to isotropic (homogeneous, small-scale) turbulence indicated by the Ozmidov frequency, the temperature variance attains the inertial subrange spectral slope of shear-induced turbulence. It is noted that despite the different characters, both dominant turbulence episodes occur when near-bottom tidal flow is near-maximum, although opposite in sign.

As the echo intensity from a single frequency instrument is an unreliable estimator of suspended matter content (e.g., Haalboom et al., 2021), net sediment-fluxes could not be quantified. However, given the two largest peaks in turbulence energy dissipation occurring every tidal period during the upslope phase of the tide, it may affect upslope net sediment transport just above the seafloor as was measured with a bottom lander along the main axis of the western branch at depths smaller than 2500 m (Amaro et al., 2016). The present observations are from one tributary and do not provide insight in the net transport through the entire canyon system. However, there are no reasons to think that other tributaries and the main channel of the easternmost branch will behave very differently than the investigated tributary. This is suggested even when taking into account that turbulence intensity varies considerably along a thalweg and over a semidiurnal period, and that the internal tide is heterogeneous between the different tributaries as shown by the modelling results by Vlasenko et al. (2016) and Aslam et al. (2018).

Enhanced turbidity pointing to elevated levels of suspended particulate matter in the water column was also observed around the deep site 1d in the CTD transect (Fig. 8). Resuspension of matter and subsequent matter dispersal in the tributary via nepheloid layers might be an important mechanism in lateral matter transport to the main thalweg. Although we do not have information on bed shear stresses, our presented data on near-bed (down to 7 m above the seafloor) turbulence demonstrate that internal wave breaking is more important than frictional shear for generating turbulence away from the seafloor and likely dominates resuspension of matter from the seafloor. Learning from previous experiments with the same equipment but with T-sensors to within 0.5 m from the seafloor (van Haren and Gostiaux, 2012), episodic large overturns do not stop at 7 m above the sloping seafloor but actually touch it. This is confirmed from numerical modelling of internal wave breaking over sloping topography by Gemmrich and Klymak (2015). The frictional law-of-the-wall is not applicable in such cases.

At the shallow site where large isothermal excursions exceeding the range of T-sensors are observed, turbulence dissipation is much more distributed over the 240 m range of observations and less affects the seafloor. No convective overturning is observed during the warming phase. The character of internal wave and turbulence is identical over the range of observations, with slightly more variance and higher tidal harmonics in the lower 100 m above the sea floor. The temperature variance changes slope from −2 (internal wave slope) to −5/3 (shear-induced turbulence subrange) at the Ozmidov frequency that coincides with the 2-m small maximum buoyancy frequency.

Together with terrain complexity, abovementioned physical processes are also important factors determining faunal patterns in Whittard Canyon, either having a direct influence through the high current speeds or indirectly affecting food supply via resuspension and focusing of organic matter (Demopoulos et al., 2017; Pearman et al., 2020). The vertical tidal displacement as observed at both mooring stations will further replenish organic matter to the fauna over the semi-diurnal tidal cycle (van Haren et al., 2014; Hall et al., 2017), being an important mechanism to supplement food delivery from surface waters (Mohn et al., 2014).

Unfortunately, due to technical reasons our time series were limited. For future observations it is suggested to set-up a high-resolution network of moorings at short distances, also occupying the side-walls for a three-dimensional impression of the development of internal tides dissipating their energy in deep-sea canyons of the continental slope.

In summary, the two sites demonstrate the following differences:

- Larger than 100 m internal wave amplitudes at the shallow site where the thalweg seafloor slope is supercritical for semidiurnal internal tides,
- Flow intensification near the seafloor at the deep site where the slope is approximately critical for semidiurnal internal tides,
- Three episodes of enhanced turbulence are observed over a tidal period, a primary and a secondary bore during the upslope phase and convective overturning during the downslope phase,

- The primary bore and the convective overturning at the deep site show elevated turbulence reaching the seafloor with potentially most effect on sediment resuspension.

Declaration of competing interest

None.

Data availability

Data will be made available on request.

Acknowledgments

We thank captain and crew of the R/V Pelagia and NIOZ-NMF for their assistance in preparing, deploying and recovering the moorings. This study was carried out in the framework of the BYPASS? project funded by the Innovational Research Scheme of the Netherlands Organisation for Scientific Research (NWO) under grant agreement no. 016.161.360.

Appendix A. Calculating the relative acoustic echo intensity

The acoustic echo intensity needs correction for water attenuation of sound to obtain a measure for suspended matter as a function of time and depth. We followed the procedure outlined by Gostiaux and van Haren (2010), to fit a log-linear profile from acoustic theory to the noise level of the instrumentation by seeking the minimum value at each depth level (Fig. A1). It is seen, that true noise levels as in pure water are not reached in the short two-day records, and the fits are slightly different between the two mooring sites. The time-depth image of Fig. 7 is thus the echo intensity relative to the smooth fits in Fig. A1.

Appendix B. Supplementary data

Supplementary data to this article can be found online at https://doi.org/10.1016/j.csr.2022.104679.

References

Amaro, T., Huvenne, V.A.I., Allcock, A.L., Aslam, T., Davies, J.S., Danovarog, R., De Stigter, H.C., Duineveld, G.C.A., Gambi, C., Gooday, A.J., Gunton, L.M., Hall, R., Howell, K.L., Ingels, J., Kiriakoulakis, K., Kershaw, C.E., Lavaleye, M.S.S., Robert, K., Stewart, H., Van Rooij, D., White, M., Wilson, A.M., 2016. The Whittard Canyon–a case study of submarine canyon processes. Prog. Oceanogr. 146, 38–57.

Aslam, T., Hall, R.A., Dye, S.R., 2018. Internal tides in a dendritic submarine canyon. Prog. Oceanogr. 169, 20–32.

Aucan, J., Merrifield, M.A., Luther, D.S., Flament, P., 2006. Tidal mixing events on the deep flanks of Kaena Ridge, Hawaii. J. Phys. Oceanogr. 36, 1202–1219.

Cacchione, D., Wunsch, C., 1974. Experimental study of internal waves over a slope. J. Fluid Mech. 66, 223–239.

Cael, B.B., Mashayek, A., 2021. Log-skew-normality of ocean turbulence. Phys. Rev. Lett. 126, 224502.

Chalamalla, V.K., Sarkar, S., 2015. Mixing, dissipation rate, and their overturn-based estimates in a near-bottom turbulent flow driven by internal tides. J. Phys. Oceanogr. 45, 1969–1983.

Cimatoribus, A.A., van Haren, H., 2015. Temperature statistics above a deep-ocean sloping boundary. J. Fluid Mech. 775, 415–435.

Demopoulos, A.W.J., Mcclain-Counts, J., Ross, S.W., Brooke, S., Mienis, F., 2017. Food-web dynamics and isotopic niches in deep-sea communities residing in a submarine canyon and on the adjacent open slopes. Mar. Ecol. Prog. Ser. 578, 19–33.

Dillon, T.M., 1982. Vertical overturns: a comparison of Thorpe and Ozmidov length scales. J. Geophys. Res. 87, 9601–9613.

Galbraith, P.S., Kelley, D.E., 1996. Identifying overturns in CTD profiles. J. Atmos. Ocean. Technol. 13, 688–702.

Gardner, W.D., 1989. Periodic resuspension in Baltimore Canyon by focusing of internal waves. J. Geophys. Res. 94, 18185–18194.

Garrett, C., Munk, W., 1972. Space-time scales of internal waves. Geophys. Fluid Dynam. 3, 225–264.

Gemmrich, J., Klymak, J.M., 2015. Dissipation of internal wave energy generated on a critical slope. J. Phys. Oceanogr. 45, 2221–2238.

Gordon, R.L., Marshall, N.F., 1976. Submarine canyons: internal wave traps? Deep Sea Res. 3, 622–624.

Gostiaux, L., van Haren, H., 2010. Extracting meaningful information from uncalibrated backscattered echo intensity data. J. Atmos. Ocean. Technol. 27, 943–949.

Gregg, M.C., D'Asaro, E.A., Riley, J.J., Kunze, E., 2018. Mixing efficiency in the ocean. Ann. Rev. Mar. Sci 10, 443–473.

Haalboom, S., de Stigter, H., Duineveld, G., van Haren, H., Reichart, G.-J., Mienis, F., 2021. Suspended particulate matter in a submarine canyon (Whittard Canyon, Bay of Biscay, NE Atlantic Ocean): assessment of commonly used instruments to record turbidity. Mar. Geol. 434, 106439.

Hall, R.A., Alford, M.H., Carter, G.S., Gregg, M.C., Lien, R.C., Wain, D.J., Zhao, Z., 2014. Transition from partly standing to progressive internal tides in Monterey submarine canyon. Deep-Sea Res. II 104, 164–173.

Hall, R.A., Aslam, T., Huvenne, V.A.I., 2017. Partly standing internal tides in a dendritic submarine canyon observed by an ocean glider. Deep Sea Res. I 126, 73–84.

Holt, J.T., Thorpe, S.A., 1997. The propagation of high frequency internal waves in the Celtic Sea. Deep Sea Res. I 44, 2087–2116.

Hosegood, P., Bonnin, J., van Haren, H., 2004. Solibore-induced sediment resuspension in the faeroe-shetland channel. Geophys. Res. Lett. 31, L09301. https://doi.org/10.1029/2004GL019544.

Hotchkiss, F.S., Wunsch, C., 1982. Internal waves in Hudson Canyon with possible geological implications. Deep Sea Res. 29, 415–442.

Inall, M.E., Toberman, M., Polton, J.A., Palmer, M.R., Green, J.A.M., Rippeth, T.P., 2021. Shelf seas baroclinic energy loss: pycnocline mixing and bottom boundary layer dissipation. J. Geophys. Res. 126, e2020JC016528.

IOC, SCOR, IAPSO, 2010. The International Thermodynamic Equation of Seawater – 2010: Calculation and Use of Thermodynamic Properties. Intergovernmental Oceanographic Commission, Manuals and Guides No. 56, UNESCO, Paris (F), p. 131.

Klymak, J.M., Moum, J.N., 2003. Internal solitary waves of elevation advancing on a shoaling shelf. Geophys. Res. Lett. 30, 2045. https://doi.org/10.1029/2003GL017706.

Klymak, J.M., Pinkel, R., Rainville, L., 2008. Direct breaking of the internal tide near topography: Kaena Ridge, Hawaii. J. Phys. Oceanogr. 38, 380–399.

Lamb, K.G., 2004. Nonlinear interaction among internal wave beams generated by tidal flow over supercritical topography. Geophys. Res. Lett. 31, L09313. https://doi.org/10.1029/2003GL019393.

LeBlond, P.H., Mysak, L.A., 1978. Waves in the Ocean. Elsevier, pp. 602–pp.

Li, S., Li, H., 2006. Parallel AMR Code for Compressible MHD and HD Equations. Theoretical division, Los Alamos National Laboratory. T-7, MS B284. http://citeseerx.ist.psu.edu/viewdoc/summary;jsessionid=1548A302FD5C2B1DFAC1BA7A5E70605F?doi=10.1.1.694.3243. (Accessed 14 November 2021).

Lo Iacono, C., Guillen, J., Guerrero, Q., Duran, R., Wardell, C., Hall, R.A., Aslam, T., Carter, G.D.O., Gales, J.A., Huvenne, V.A.I., 2020. Bidirectional bedform fields at the head of a submarine canyon (NE Atlantic). Earth Planet Sci. Lett. 542, 116321.

Maier, K.L., Rosenberger, K.J., Paull, C.K., Gwiazda, R., Gales, J., Lorenson, T., Barry, J. P., Talling, P.J., Mcgann, M., Xu, J., Lundsten, E., Anderson, K., Litvin, S.Y., Parsons, D.R., Clare, M.A., Simmons, S.M., Sumner, E.J., Cartigny, M.J.B., 2019. Sediment and organic carbon transport and deposition driven by internal tides along Monterey Canyon, offshore California. Deep-Sea Res. I 153, 103108.

Masson, D.G., Huvenne, V.A.I., De Stigter, H.C., Wolff, G.A., Kiriakoulakis, K., Arzola, R. G., Blackbird, S., 2010. Efficient burial of carbon in a submarine canyon. Geol. 38, 831–834.

Mater, B.D., Venayagamoorthy, S.K., St Laurent, L., Moum, J.N., 2015. Biases in Thorpe scale estimation of turbulence dissipation. Part I: assessments from large-scale overturns in oceanographic data. J. Phys. Oceanogr. 45, 2497–2521.

Matsumoto, Y., Hoshino, M., 2004. Onset of turbulence by a Kelvin-Helmholtz vortex. Geophys. Res. Lett. 31, L02807. https://doi.org/10.1029/2003GL018195.

Mohn, C., Rengstorf, A., White, M., Duineveld, G., Mienis, F., Soetaert, K., Grehan, A., 2014. Linking benthic hydrodynamics and cold-water coral occurrences: A high-resolution model study at three cold-water coral provinces in the NE Atlantic. Progr. Oceanogr. 122, 92–104.

Nash, J.D., Kunze, E., Toole, J.M., Schmitt, R.W., 2004. Internal tide reflection and turbulent mixing on the continental slope. J. Phys. Oceanogr. 34, 1117–1134.

Nash, J.D., Alford, M.H., Kunze, E., Martini, K., Kelly, S., 2007. Hotspots of deep ocean mixing on the Oregon continental slope. Geophys. Res. Lett. 34, L01605. https://doi.org/10.1029/2006GL028170.

Oakey, N.S., 1982. Determination of the rate of dissipation of turbulent energy from simultaneous temperature and velocity shear microstructure measurements. J. Phys. Oceanogr. 12, 256–271.

Palanques, A., Puig, P., Latasa, M., Scharek, R., 2009. Deep sediment transport induced by storms and dense shelf-water cascading in the northwestern Mediterranean basin. Deep-Sea Res. I 56, 425–434.

Palmer, M.R., Stephenson, G.R., Inall, M.E., Balfour, C., Düsterhus, A., Green, J., 2015. Turbulence and mixing by internal waves in the Celtic Sea determined from ocean glider microstructure measurements. J. Mar. Syst. 144, 57–69.

Pawar, S.S., Arakeri, J.H., 2016. Kinetic energy and scalar spectra in high Rayleigh number axially homogeneous buoyancy driven turbulence. Phys. Fluids 28, 065103.

Pearman, T.R.R., Robert, K., Callaway, A., Hall, R., Lo Iacono, C., Huvenne, V.A.I., 2020. Improving the predictive capability of benthic species distribution models by incorporating oceanographic data - towards holistic ecological modelling of a submarine canyon. Prog. Oceanogr. 184, 102338.

Petruncio, E.T., Rosenfeld, L.K., Paduan, J.D., 1998. Observations of the internal tide in Monterey Canyon. J. Phys. Oceanogr. 28, 1873–1903.

Pingree, R.D., Mardell, G.T., New, A.L., 1986. Propagation of internal tides from the upper slopes of the Bay of Biscay. Nature 321, 154–158.

Puig, P., Palanques, A., Martin, J., 2014. Contemporary sediment-transport processes in submarine canyons. Ann. Rev. Mar. Sci 6, 53–77.

Robertson, C.M., Demopoulos, A.W.J., Bourque, J.R., Mienis, F., Duineveld, G.C.A., Lavaleye, M.S.S., Koivisto, R.K.K., Brooke, S.D., Ross, S.W., Rhode, M., Davies, A.J., 2020. Submarine canyons influence macrofaunal diversity and density patterns in the deep-sea benthos. Deep-Sea Res. I 159, 103249.

St Laurent, L.C., Toole, J.M., Schmitt, R.W., 2001. Buoyancy forcing by turbulence above rough topography in the Brazil Basin. J. Phys. Oceanogr. 31, 3476–3495.

Tennekes, H., Lumley, J.L., 1972. A First Course in Turbulence. The MIT Press, p. 293.

Thurnherr, A.M., Clément, L., St Laurent, L., Ferrari, R., Ijichi, T., 2020. Transformation and upwelling of bottom water in fracture zone valleys. J. Phys. Oceanogr. 50, 715–726.

Thorpe, S.A., 1977. Turbulence and mixing in a Scottish loch. Phil. Trans. Roy. Soc. Lond. 286, 125–181.

Thorpe, S.A., 1987. Current and temperature variability on the continental slope. Phil. Trans. Roy. Soc. Lond. 323, 471–517.

van Haren, H., 2006. Nonlinear motions at the internal tide source. Geophys. Res. Lett. 33, L11605. https://doi.org/10.1029/2006GL025851.

van Haren, H., 2015. Instability observations associated with wave breaking in the stable-stratified deep-ocean. Physica D 292–293, 62–69.

van Haren, H., 2017. Exploring the vertical extent of breaking internal wave turbulence above deep-sea topography. Dynam. Atmos. Oceans 77, 89–99.

van Haren, H., 2018. Philosophy and application of high-resolution temperature sensors for stratified waters. Sensors 18, 3184. https://doi.org/10.3390/s18103184.

van Haren, H., 2019. Deep-ocean inertial subrange small bandwidth coherence and Ozmidov-frequency separation. Phys. Fluids 31, 066603.

van Haren, H., Gostiaux, L., 2009. High-resolution open-ocean temperature spectra. J. Geophys. Res. 114, C05005. https://doi.org/10.1029/2008JC004967.

van Haren, H., Gostiaux, L., 2012. Detailed internal wave mixing above a deep-ocean slope. J. Mar. Res. 70, 173–197.

van Haren, H., Dijkstra, H.A., 2021. Convection under internal waves in an alpine lake. Environ. Fluid Mech. 21, 305–316.

van Haren, H., Mienis, F., Duineveld, G.C.A., Lavaleye, M.S.S., 2014. High-resolution temperature observations of a trapped nonlinear diurnal tide influencing cold-water corals on the Logachev mounds. Prog. Oceanogr. 125, 16–25.

van Haren, H., Cimatoribus, A.A., Gostiaux, L., 2015. Where large deep-ocean waves break. Geophys. Res. Lett. 42, 2351–2357. https://doi.org/10.1002/2015GL063329.

Vetter, E.W., Smith, C.R., De Leo, F.C., 2010. Hawaiian hotspots: enhanced megafaunal abundance and diversity in submarine canyons on the oceanic islands of Hawaii. Mar. Ecol. 31, 183–199.

Vlasenko, V., Stashchuk, N., Inall, M.E., Hopkins, J.E., 2014. Tidal energy conversion in a global hot spot: on the 3-D dynamics of baroclinic tides at the Celtic Sea shelf break. J. Geophys. Res. 119, 3249–3265.

Vlasenko, V., Stashchuk, N., Inall, M.E., Porter, M., Aleynik, D., 2016. Focusing of baroclinic tidal energy in a canyon. J. Geophys. Res. 121, 2824–2840.

Warhaft, Z., 2000. Passive scalars in turbulent flows. Annu. Rev. Fluid Mech. 32, 203–240.

Wilson, A.M., Raine, R., Mohn, C., White, M., 2015. Nepheloid layer distribution in the Whittard Canyon, NE Atlantic Margin. Mar. Geol. 367, 130–142.

Winters, K.B., 2015. Tidally driven mixing and dissipation in the boundary layer above steep submarine topography. Geophys. Res. Lett. 42, 7123–7130. https://doi.org/10.1002/2015GL064676.

Zhao, Z., Alford, M.H., Lien, R.C., Gregg, M.C., Carter, G.S., 2012. Internal tides and mixing in a submarine canyon with time-varying stratification. J. Phys. Oceanogr. 42, 2121–2142.